Probing the cluster structure of ^{6}Li with the ^{6}Li + ^{12}C nuclear reaction at 68 MeV*

B. A. Urazbekov[1,2]   E. K. Almanbetova[3]   A. Azhibekov[3,4]   B. S. Baimurzinova[5]   K. Dyussebayeva[6]

T. Issatayev[2,3†]   D. M. Janseitov[2]   S. M. Lukyanov[3]   Yu. E. Penionzhkevich[3]

K. Mendibayev[2,3]   T. K. Zholdybayev[2,6]

[1]Gumilyov Eurasian National University, 2 Satpayev Str., Astana 010000, Kazakhstan
[2]Institute of Nuclear Physics, 1 Ibragimov Str., Almaty 050032, Kazakhstan
[3]Flerov Laboratory of Nuclear Reactions, JINR, 20 Joliot Curie Str., Dubna 141980, Russia
[4]Korkyt-ata State University, 29A Aiteke-Byi Str, Kyzylorda 120000, Kazakhstan
[5]SDU University, 1/1 Abylaikhan Str., Kaskelen, Almaty 040900, Kazakhstan
[6]Al-Farabi Kazakh National University, 71 Al-Farabi Ave., Almaty 050040, Kazakhstan

Abstract: This study presents a combined experimental and theoretical investigation of the ^{6}Li + ^{12}C nuclear reaction at a laboratory energy of 68 MeV. The reaction products are identified via the standard ΔE–E technique. Angular distributions are constructed for the elastic, inelastic, and deuteron transfer channels by detecting emitted particles – ^{6}Li and α. Elastic and inelastic scattering of ^{6}Li off ^{12}C are analyzed using the optical model and coupled channels approaches, with the interaction described by a double-folding potential. This potential is calculated based on the three-body wave function of ^{6}Li. Pronounced coupled-channel effects that modify the potential and allow accurate reproduction of the experimental cross sections are observed. The resulting polarized potentials provide a more precise description of the initial-state interaction for further reaction modeling. The deuteron transfer channel, ^{12}C(^{6}Li, α)^{14}N, is studied using the coupled reaction channels method. The coupling between the transfer and elastic channels is implemented using the three-body wave function of ^{6}Li. As an alternative, a regular wave function constructed with a phenomenological Woods–Saxon potential is also employed. Comparison between the calculated differential cross sections and experimental data reveals a more complex and nuanced reaction mechanism, which supports the cluster structure of ^{6}Li.

Keywords: three-body model, double-folding potential, coupled channels, cluster structure, optical model, coupled-reaction channels

I. INTRODUCTION

With the development of detection systems, increase in computing power, and emergence of new theoretical approaches, the study of light nuclei remains a central topic in nuclear structure research.

In particular, the ^{6}Li nucleus is a light nucleus characterized by a well-established cluster structure, typically modeled as a bound system of an alpha particle and a deuteron ($\alpha + d$). This configuration plays a crucial role in the internal dynamics of the nucleus and distinguishes ^{6}Li from other light systems [1−3]. Due to its relatively weak binding energy and extended spatial correlations between constituents, a full three-body description is often necessary to capture its physical properties, as simpler two-body models may neglect essential degrees of freedom. As such, ^{6}Li represents a valuable system for exploring clustering phenomena and few-body interactions in nuclear physics. Recent studies, both theoretical and experimental, provide further evidence of these unique features [4−7].

The clustered nature of ^{6}Li has a significant impact on its behavior in nuclear reactions, including elastic and inelastic scattering and cluster transfer processes. Experimental studies involving ^{6}Li beams have revealed features that require theoretical approaches to explicitly account for cluster dynamics. In particular, the use of realistic three-body wave functions has been shown to improve agreement with reaction observables [8−10]. Thus, investigations of ^{6}Li reactions provide key insights into

the interplay between nuclear structure and reaction mechanisms and serve as a testing ground for modern few-body and cluster-based theoretical models [11−14]. In particular, in Ref. [8], tests were performed on the ^{6}Li nucleus to validate the three-body model and the adopted interactions. The effects of the Pauli principle, various NN and α–N potentials, and the convergence and structure of the wave functions were considered. Binding energies, radii, the component composition of the wave functions in the LS coupling scheme, and the hypermomentum decomposition were calculated.

The internal structure of light nuclei also plays an important role in shaping nuclear reaction mechanisms [15−19], especially when one of the colliding nuclei possesses a well-established cluster structure. In Ref. [20], a four-body model (target nucleus + α-core + two valence neutrons) was developed and applied to describe two-neutron transfer reactions involving Borromean nuclei, primarily ^{6}He, and based on this, data on ^{6}He–^{4}He collisions were analyzed. A realistic three-body bound-state wave function of ^{6}He, obtained through expansion over hyperspherical harmonics with inclusion of n–n and n–α interactions, was used in the calculations. The results showed that the cross sections strongly depend on the internal structure of ^{6}He; the calculated cross sections indicated that the "dineutron" component—where two neutrons are close to each other outside the α-core—gives the dominant contribution to the transfer, whereas the "cigarlike" configuration – where the two neutrons are much farther apart than the α-core – is noticeable only at larger angles.

Motivated by these findings, we aim to explore the cluster structure of ^{6}Li in the nuclear reaction ^{6}Li + ^{12}C at a laboratory energy of 68 MeV. In particular, our interest focuses on the deuteron-transfer channels originating from the ^{6}Li nucleus. Based on the well-established cluster structure, we employ a three-body model of ^{6}Li. This study focuses on two central questions: in what way the cluster transfer contributes to the nuclear reaction and how the overall reaction mechanism is affected when the three-body structure is not considered.

This study is a continuation of a series of studies [21−23] devoted to the investigation of cluster effects in nuclear reactions. In this context, the present study extends previous analyses by focusing on the ^{6}Li + ^{12}C reaction at 68 MeV, with particular attention to the deuteron-transfer channel.

The remainder of this paper is organized as follows. In Section II, we describe the experimental procedure, measurement conditions, and methods used to obtain and process the data. Section III introduces the three-body wave function employed in this study and outlines the procedure used to derive the nuclear matter density distribution of ^{6}Li, which serves as input for the subsequent reaction calculations. Section IV is devoted to interpreting the calculated results for elastic and inelastic scattering in comparison with the experimental cross sections. Section V focuses on the analysis of the experimental data for the deuteron-transfer reaction and its correlation with the three-body structure of ^{6}Li. Finally, the main conclusions and outlook are summarized in Section VI.

II. EXPERIMENTAL PROCEDURE

Experiments with a ^{6}Li beam on a ^{12}C target were conducted at the Flerov Laboratory of Nuclear Reactions, Joint Institute for Nuclear Research, Dubna, Russia. A ^{6}Li beam with an energy of 68 MeV was accelerated by the U-400 cyclotron and directed to the reaction chamber of the high-resolution MAVR [16], spectrometer. The magnetic optics of the U-400 cyclotron, combined with a system of diaphragms, formed the beam profile. A profilometer installed upstream of the reaction chamber confirmed a beam spot of approximately 5 mm × 5 mm on the target, with a typical current of 30 nA. The beam charge was monitored using a Faraday cup and cross-checked via elastic scattering measurements.

The beam was incident on a self-supporting ^{12}C foil with a thickness of 5 μm and purity greater than 99%. No contaminant isotopes were observed in the energy spectra.

Particle identification was performed using the ΔE–E technique, measuring energy loss in the first two detector layers and the residual energy in the third. Four three-layer silicon telescopes were employed with thicknesses of 50 μm–100 μm–3200 μm for forward angles and 12 μm–700 μm–3200 μm for backward angles. The solid angle and angular acceptance were approximately 0.03 msr and 0.35° for forward-angle telescopes and 0.2 msr and 0.9° for backward-angle telescopes, respectively. This configuration enabled clear identification of reaction products over a wide energy range, from helium to boron isotopes.

Examples of particle identification matrices obtained with one of the telescopes are shown in Fig. 1, demonstrating excellent separation of all detected species. By selecting appropriate gates on the particle loci in the identification matrix (Fig. 1), energy spectra for various reaction channels were extracted. Figure 2 (a) presents the energy spectrum for outgoing ^{6}Li particles, showing peaks corresponding to elastic scattering from the ^{12}C ground state and inelastic scattering to its excited states. Similarly, Fig. 2 (b) shows the excitation energy spectrum for the ^{12}C(^{6}Li, α)^{14}N transfer reaction, where the ejectiles are α particles. The spectrum reveals several populated states in the residual ^{14}N nucleus, though the present analysis focuses only on ground-state transition.

The energy spectra and angular distributions were measured using an inclusive method. The overall energy resolution was primarily influenced by the intrinsic en-
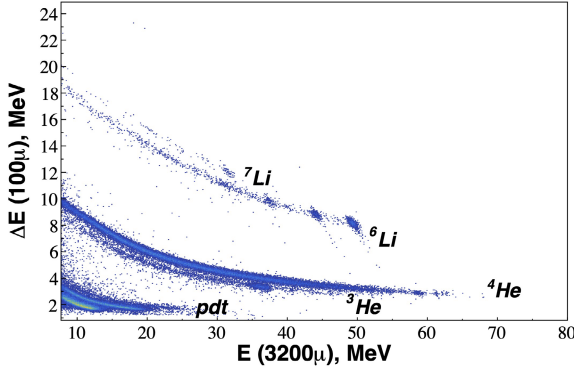
Fig. 1. (color online) Typical two-dimensional particle identification spectrum (ΔE–E) for the reaction products of the ^{6}Li + ^{12}C reaction, measured at a laboratory angle of $\theta_{lab} = 26°$. The data were obtained using one of the silicon telescopes. The loci corresponding to different isotopes, including ^{4}He, ^{6}Li, and ^{7}Li, are clearly separated.

ergy spread of the ^{6}Li beam and uncertainties in energy loss within the ^{12}C target. The resulting energy resolution was approximately 500 keV for ejectiles with $Z = 1$–3 and approximately 1 MeV for those with $Z = 4$–6.

III. THE THREE BODY MODEL

In this study, the ^{6}Li nucleus is modeled as a three-body system consisting of one α particle, proton, and neutron. The quantum state of this system is described by the wave function $\Psi^{JM}(x,y)$, where J is the total angular momentum, and M is its projection. The wave function is constructed using the Jacobi relative coordinates x and y, which eliminate the center-of-mass motion. The coordinate configuration is illustrated in Fig. 3 (a). The three-body wave function is constructed based on pairwise interactions in the α–N and N–N subsystems. Specifically, the α–N interaction is modeled using a parity-dependent potential fitted to reproduce scattering data [24]. This potential accurately reproduces phase shifts for proton–α scattering up to 20 MeV. The N–N interaction is described using the Reid soft-core potential [25]. It is worth noting that the α–N system contains a forbidden state in the S-wave channel. This issue is addressed using the orthogonalising pseudo-potentials technique [26], which projects out the forbidden state during the variational calculation.

The wave function $\Psi^{JM}(x,y)$ used was adopted from Ref. [13], as it provides a good description of ^{6}Li, especially its low-lying energy spectrum and electromagnetic properties, which makes it a physically well-grounded and reliable basis for further nuclear reaction calculations.

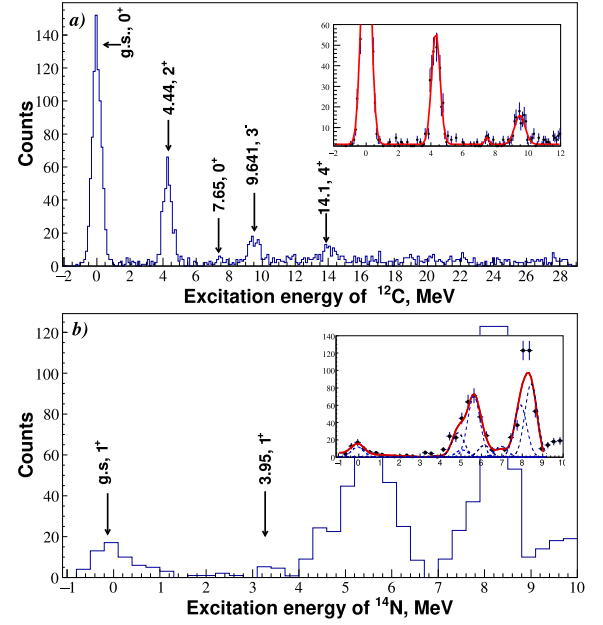The nuclear matter density distribution of ^{6}Li in the three-body model is written as [27]

Fig. 2. (color online) (a) Excitation energy spectrum of ^{12}C obtained from the ^{6}Li + ^{12}C reaction at $E_{lab} = 68$ MeV. The spectrum displays peaks corresponding to elastic scattering (g.s. 0^+) and inelastic scattering to excited states at 4.44 MeV (2^+), 7.65 MeV (0^+), 9.641 MeV (3^-), and 14.1 MeV (4^+). The inset illustrates the peak fitting procedure used to extract the yields for each state. (b) Excitation energy spectrum for the ^{12}C(^{6}Li, α)^{14}N reaction channel at $E_{lab} = 68$ MeV. The ground state (g.s. 1^+), which is the focus of the theoretical analysis in this study, is clearly identified. The spectrum also reveals the population of the 3.95 MeV state and several higher-lying states. The inset shows a multi-peak fit used to extract the contributions from individual excited states.

$$\rho(r) = \sum_i \rho_i(r), \tag{1}$$

where the sum is taken over all the clusters in the system. For each cluster, the density is calculated as

$$\rho_i(r) = \langle \Psi^{JM}(x,y)| \hat{\rho}_i |\Psi^{JM}(x,y)\rangle, \tag{2}$$

where $\hat{\rho}_i$ is the density operator, defined as

$$\hat{\rho}_i = \begin{cases} \delta(y - y_0 r), & i \text{ nucleon} \\ \rho_\alpha(y - y_0 r), & \text{for } i\ \alpha \text{ particle.} \end{cases} \tag{3}$$

where y_0 takes the value 5/6 for nucleons and 1/3 for the α-cluster. In this study, nucleons are treated as point-like, whereas the α particle is assumed to have an internal structure described by a Gaussian distribution that reproduces the root-mean-square (rms) radius of 1.461 fm [28]. To facilitate the treatment of nucleons, the Jacobi
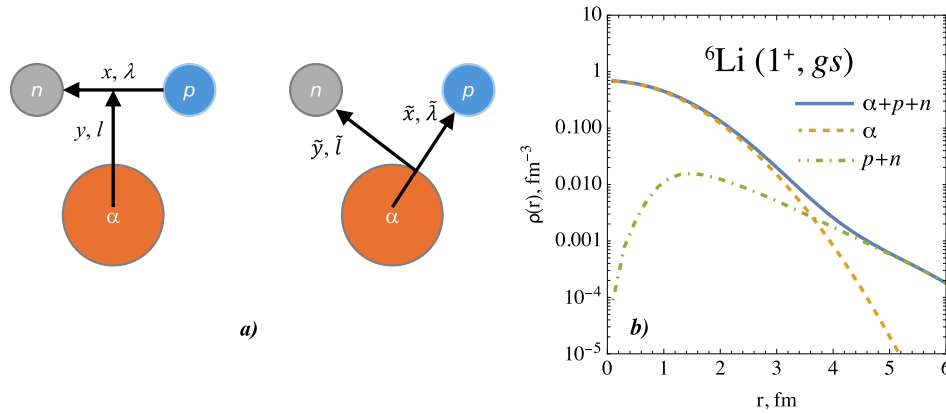
Fig. 3. (color online) *a)* Schematic representation of the three-body model of ^{6}Li with relative Jacobi coordinates x and y for the system of an α particle and two nucleons. The "*T*"-type configuration is shown on the left and the "*Y*"-type on the right. *b)* Nuclear matter density distribution functions $\rho(r)$ for ^{6}Li calculated within the three-body model: solid line – total density, dashed line – α cluster, dot-dashed line – $p+n$ cluster.

coordinate system is transformed from the "*T*"-type to the "*Y*"-type (see Fig. 3 (a)).

The nuclear matter density distribution functions were calculated with the three body wave function parameters taken from Ref. [29] and are shown in Fig. 3 (*b*) in terms of clusters contributions. In this study, we employed the *S*-wave component of the three-body configuration set, as it accounts for the dominant contribution, approximately 89% of the total weight. A distinctive feature of the obtained results is the extended tail of the density distribution. This behavior is due to the properties of the valence nucleons in the three-body system. In particular, the density of the α cluster decreases rapidly with increasing radius r, while the density of the valence nucleons decreases more slowly. This indicates a stronger contribution from the $p+n$-cluster component. Another notable feature is a local maximum in the nucleon density at $r \approx 1.5$ fm, which reflects the fact that the valence nucleons are spatially separated from the center of mass.

Using the obtained nuclear matter density distribution for ^{6}Li, we can estimate its rms radius. The calculated rms radius is 2.49 fm, which falls within the range of values 2.54 ± 0.03 reported in Ref. [30].

IV. ELASTIC AND INELASTIC CHANNELS

Optical Model

The differential cross sections of the elastic scattering of ^{6}Li from the ^{12}C nucleus at the laboratory energy of 68 MeV are treated within the optical model (OM) framework. The optical potential used in the OM calculations was taken in the form

$$U(R) = -V(R) - iW(R) + V^C(R), \qquad (4)$$

where R is the distance between the ^{6}Li and ^{12}C nuclei;

V, W are the real and imaginary volume potential terms, respectively; and V^C is the Coulomb potential.

The real volume potential $V(R)$ can be obtained within the double-folding model [28]:

$$V(R) \equiv N_R V^{DF}(R) = \int \int d\boldsymbol{r}_p d\boldsymbol{r}_t \rho_p(\boldsymbol{r}_p)$$
$$\times V_{NN}(\boldsymbol{R} - \boldsymbol{r}_p + \boldsymbol{r}_t)\rho_t(\boldsymbol{r}_t), \qquad (5)$$

where $\boldsymbol{r}_p$ and $\boldsymbol{r}_t$ are internal coordinates of the projectile and target nuclei, respectively; ρ_p and ρ_t are their nuclear matter density distributions; V_{NN} is the effective nucleon–nucleon interaction; and N_R is a free parameter adjusted to reproduce the observed reaction dynamics. In this study, the projectile density ρ_p is obtained from the three-body wave function of ^{6}Li (Eq. (1)), whereas the target density ρ_t is modeled with a parametrized Fermi distribution for ^{12}C, constrained by the experimental rms charge radius of 2.47 fm (see, *e.g.*, Ref. [31]).

The imaginary part of the optical potential can be represented by a Woods–Saxon form [32]:

$$W(R) = \frac{W_0}{1 + \exp\left(\dfrac{R - R_W}{a_W}\right)}, \qquad (6)$$

where W_0 is the depth of the potential, R_W is the radius parameter, and a_W is the diffuseness parameter; the Coulomb interaction is taken as the interaction of a point-charge with a uniformly charged sphere,

$$V^C(R) = \begin{cases} \dfrac{Z_1 Z_2 e^2}{2R_C}\left(3 - \dfrac{R^2}{R_C^2}\right), & \text{for } R \leq R_C, \\[4mm] \dfrac{Z_1 Z_2 e^2}{R}, & \text{for } R > R_C. \end{cases} \qquad (7)$$

The double-folding (DF) potential is obtained using the Python-based code BiFOLD, which implements the nuclear density functions mentioned above and the nucleon–nucleon interaction of the CDM3Y-6 type reported in Ref. [33]. The resulting DF potential is then used to analyze the elastic scattering channel within the OM using the FRESCO code [34]. The imaginary part of the DF potential is fitted by χ^2 minimization, with the initial global parameters taken from Ref. [35] and listed in Table 1.

The results of numerical calculations within the OM for the elastic scattering reaction ^{12}C(^{6}Li, ^{6}Li)^{12}C at a laboratory energy of 68 MeV are compared with the experimental data in Fig. 4. The DF potential used within the OM reproduces the experimental data well, except in the angular region beyond 90°. The good agreement at forward angles confirms the validity of the modeled interactions between the colliding nuclei based on the three-body structure of the ^{6}Li nucleus.

Coupled channels

One specific feature of the results is the remaining discrepancy at backward angles in the elastic scattering channel. Indeed, when the coupled channels (CC) approach is employed together with the coupling scheme shown in Fig. 5, which also includes backward couplings in addition to the Distorted Wave Born Approximation (DWBA), the calculated differential cross sections reproduce the experimental elastic scattering data even at backward angles, providing a more accurate overall description. Detailed analyses have shown that a strong CC effect arises primarily from the inelastic scattering channel at 4.44 MeV, which leads to an increased elastic scattering cross section at angles beyond 90°.

Electromagnetic transition strengths for Coulomb excitation coupling were adopted from Ref. [36]. The deformation length for the transition in ^{12}C from the ground state to the first excited 2^+ state at 4.44 MeV reproduces the experimental differential cross sections well when taken in the range of 1.75 ± 0.15 fm. The obtained deformation length lies within the values reported for ^{4}He projectiles [37], namely, 1.95 fm at a laboratory energy of 139 MeV and 1.37 fm at a laboratory energy of 65 MeV. Particular interest is also associated with the deformation length for the octupole transition in ^{12}C, *i.e.*, from the

ground state to the excited state at 9.64 MeV. The coupled–channels analysis shows that the value of 0.70 ± 0.07 fm provides a good description of the experimental cross sections. Indeed, this value is consistent with the results obtained using the deformation parameter $\beta_3 = 0.26$ [38], which generates the deformation length $\delta_3 = \beta_3 \cdot 1.2 A^{1/3} = 0.71$ fm. These results were obtained within the CC method with the same projectile at laboratory energies of 60 and 77 MeV.

The CC model provides a satisfactory reproduction of the experimental data, except at angles beyond 90° for the channel with 4.44 MeV excitation and beyond 60° for the
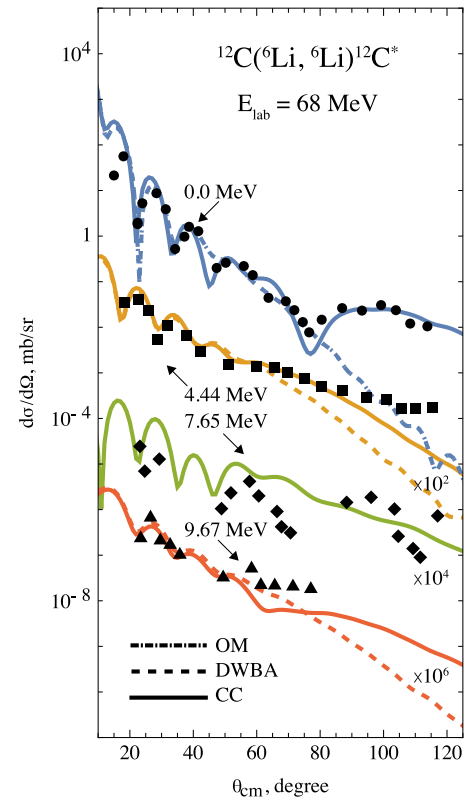
Fig. 4. (color online) Experimental angular distributions of elastic (circles) and inelastic scattering at excitation energies of 4.44 MeV (squares), 7.65 MeV (diamonds), and 9.67 MeV (triangles) resulting from the ^{6}Li + ^{12}C* reaction at $E_{lab} = 68$ MeV, shown in comparison with different model calculations: solid line – CC method, dashed – DWBA, dash-dotted – OM.

Table 1. Optical potential parameters used in the OM, CC, and CRC calculations.

	N_R	V_0/MeV	$r_V^{a)}$/fm	a_V/fm	W_0/MeV	$r_W^{a)}$/fm	a_W/fm	$r_C^{a)}$/fm	χ^2/N
^{6}Li+^{12}C	0.61	–	–	–	23.35	1.528	0.773	1.67	7.41
	0.69[b)]				15.31[b)]				
$\alpha+^{14}$N	–	187.7	0.880	0.875	35.0	0.516	1.313	1.35	8.32
		176.6 [c)]			50.0[c)]				

[a)] $r_i = R_i A_t^{-1/3}$; [b)] used in the CC and CRC; [c)] used in the CRC.

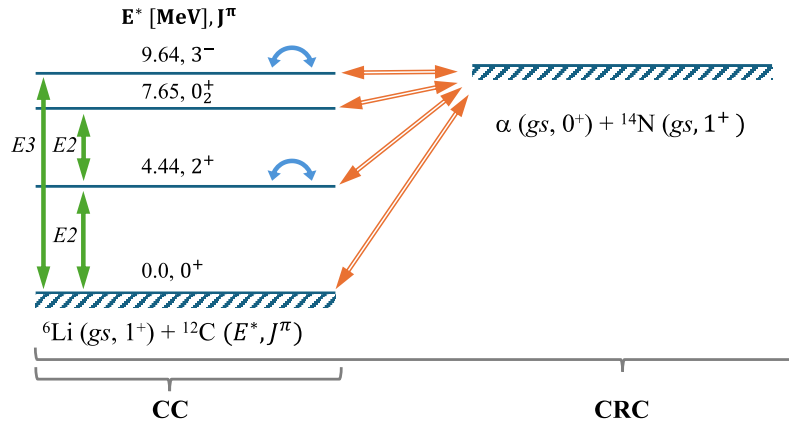**Fig. 5.**   (color online) Coupling scheme used in the CC calculations for ^{12}C(^{6}Li, ^{6}Li')^{12}C* inelastic scattering and in the CRC calculations for ^{12}C(^{6}Li, α)^{14}N. Double-headed arrows indicate $E\lambda$ transitions, backward-pointing arrows indicate spin-reorientation, and double-lined arrows indicate reaction transitions.

channel with 9.67 MeV excitation. This discrepancy likely arises from omitted couplings to higher-lying states in the CC coupling scheme.

The inelastic channel with 7.65 MeV excitation also deserves special attention, as it corresponds to the well-known Hoyle state. The coupling does not proceed directly from the ground state due to the forbidden $E0$ transition (see Fig. 5) but rather through the intermediate excited state at 4.44 MeV. As a result, the definition of the deformation parameter with respect to the ground state loses its physical meaning. This most likely explains why the present model is insufficient to reproduce the overall angular distribution for this transition. The analysis clearly indicates the involvement of an additional inelastic mechanism, whose interference with the considered channels would provide a more complete description. For a more accurate and comprehensive treatment of this state, a more advanced modeling framework is required, one that explicitly incorporates the 3α cluster structure.

Explicitly implemented within the CC framework, inelastic channels lead to noticeable coupled-channel effects. These effects cause a 13% increase in the depth of the DF potential and 28% reduction in the depth of the imaginary part of the optical potential (see Table 1). The modified (or polarized) potential represents how the interaction between the colliding nuclei is effectively changed by the coupling to inelastic excitation channels. Such potentials yield a more accurate representation of the initial-state interaction and are consistent with previous findings in Refs. [21, 39–40].

V. DEUTERON TRANSFER CHANNEL

Coupled Reaction Channels

The nuclear reaction ^{12}C(^{6}Li, α)^{14}N is analyzed within the framework of the coupled-reaction-channels (CRC) approach [34]. The coupling scheme employed in the CRC framework is shown in Fig. 5. In the analysis, the

initial-state interaction is chosen to be the polarised double-folding (DF) potential, while the final-state interaction is represented by the Woods–Saxon potential for both the real and imaginary parts. The parameters were adjusted to reproduce the experimental differential cross sections for α + ^{14}N elastic scattering at a laboratory energy of 54 MeV [41]. The real part is expressed as follows:

$$V(R) = \frac{V_0}{1 + \exp\left(\dfrac{R - R_V}{a_V}\right)}, \tag{8}$$

while the imaginary volume potential has the same shape as that used for the ^{6}Li + ^{12}C system (Eq. (6)).

In the calculations, the coupling potentials were constructed using the prior form. The potential of the final-state interaction was chosen to be the core-core potential in the remnant part, as this type of potential is observed to be more dependent on the projectile than the target nuclei.

Two-nucleon spectroscopic amplitudes for the target overlaps $\langle ^{14}\text{N} \mid ^{12}\text{C} \rangle$ were calculated using the KSHELL code [42] utilizing the effective nucleon-nucleon interaction [43]. The results of the calculations are summarized in Table 2. To incorporate the calculated amplitudes into the reaction model, they were transformed into the corresponding cluster coupling scheme (*e.g.*, see Ref. [34]).

The relative-motion wave functions were generated using a Woods–Saxon potential (Eq. (8)) with a radius parameter of 1.25 fm and diffuseness of 0.65 fm, while the depth was adjusted to reproduce the experimental binding energy.

For the projectile overlaps, the relative-motion wave function of the α + d system was obtained by projecting the internal s-state of the deuteron onto the three-body wave function as follows:

Table 2. Two-nucleon spectroscopic amplitudes, A^{SM}, used in the CRC calculations for the overlaps $\langle^{14}\mathrm{N}(J_f)|^{12}\mathrm{C}(J_i)\rangle$. The transferred proton and neutron are assumed to occupy the shells $nlj(\rho)$ and $nlj(\eta)$, respectively, and are coupled to the total angular momentum J.

J_f	J_i	$nlj(\rho)$	$nlj(\eta)$	J	A^{SM}	J_f	J_i	$nlj(\rho)$	$nlj(\eta)$	J	A^{SM}
1^+	0_1^+	$0p_{1/2}$	$0p_{1/2}$	1	0.58269	1^+	2^+	$0d_{3/2}$	$0d_{5/2}$	3	0.00407
1^+	0_2^+	$0p_{1/2}$	$0p_{1/2}$	1	0.62634	1^+	2^+	$0d_{3/2}$	$1s_{1/2}$	1	0.06353
1^+	0_1^+	$0p_{1/2}$	$0p_{3/2}$	1	0.08622	1^+	2^+	$0d_{3/2}$	$1s_{1/2}$	2	−0.00157
1^+	0_2^+	$0p_{1/2}$	$0p_{3/2}$	1	−0.04502	1^+	2^+	$0d_{5/2}$	$0d_{3/2}$	1	−0.13446
1^+	0_1^+	$0p_{3/2}$	$0p_{1/2}$	1	−0.08623	1^+	2^+	$0d_{5/2}$	$0d_{3/2}$	2	0.04508
1^+	0_2^+	$0p_{3/2}$	$0p_{1/2}$	1	0.04508	1^+	2^+	$0d_{5/2}$	$0d_{3/2}$	3	−0.00406
1^+	0_1^+	$0p_{3/2}$	$0p_{3/2}$	1	−0.09427	1^+	2^+	$0d_{5/2}$	$0d_{5/2}$	1	0.09096
1^+	0_2^+	$0p_{3/2}$	$0p_{3/2}$	1	0.02279	1^+	2^+	$0d_{5/2}$	$0d_{5/2}$	2	0.00001
1^+	0_1^+	$0d_{3/2}$	$0d_{3/2}$	1	0.03725	1^+	2^+	$0d_{5/2}$	$0d_{5/2}$	3	−0.00022
1^+	0_2^+	$0d_{3/2}$	$0d_{3/2}$	1	0.01689	1^+	2^+	$0d_{5/2}$	$1s_{1/2}$	2	0.00025
1^+	0_1^+	$0d_{3/2}$	$0d_{5/2}$	1	0.03982	1^+	2^+	$0d_{5/2}$	$1s_{1/2}$	3	−0.00586
1^+	0_2^+	$0d_{3/2}$	$0d_{5/2}$	1	0.01663	1^+	2^+	$1s_{1/2}$	$0d_{3/2}$	1	−0.06353
1^+	0_1^+	$0d_{3/2}$	$1s_{1/2}$	1	0.02205	1^+	2^+	$1s_{1/2}$	$0d_{3/2}$	2	−0.00156
1^+	0_2^+	$0d_{3/2}$	$1s_{1/2}$	1	0.01008	1^+	2^+	$1s_{1/2}$	$0d_{5/2}$	2	−0.00023
1^+	0_1^+	$0d_{5/2}$	$0d_{3/2}$	1	−0.03981	1^+	2^+	$1s_{1/2}$	$0d_{5/2}$	3	−0.00587
1^+	0_2^+	$0d_{5/2}$	$0d_{3/2}$	1	−0.01662	1^+	2^+	$1s_{1/2}$	$1s_{1/2}$	1	0.12143
1^+	0_1^+	$0d_{5/2}$	$0d_{5/2}$	1	0.00526	1^+	3^-	$0p_{1/2}$	$0d_{3/2}$	2	−0.00874
1^+	0_2^+	$0d_{5/2}$	$0d_{5/2}$	1	0.00847	1^+	3^-	$0p_{1/2}$	$0d_{5/2}$	2	−0.02594
1^+	0_1^+	$1s_{1/2}$	$0d_{3/2}$	1	−0.02204	1^+	3^-	$0p_{1/2}$	$0d_{5/2}$	3	−0.04672
1^+	0_2^+	$1s_{1/2}$	$0d_{3/2}$	1	−0.01008	1^+	3^-	$0p_{3/2}$	$0d_{3/2}$	2	0.03579
1^+	0_1^+	$1s_{1/2}$	$1s_{1/2}$	1	−0.04015	1^+	3^-	$0p_{3/2}$	$0d_{3/2}$	3	−0.00462
1^+	0_2^+	$1s_{1/2}$	$1s_{1/2}$	1	−0.03097	1^+	3^-	$0p_{3/2}$	$0d_{5/2}$	2	0.02006
1^+	2^+	$0p_{1/2}$	$0p_{1/2}$	1	−0.20164	1^+	3^-	$0p_{3/2}$	$0d_{5/2}$	3	0.00563
1^+	2^+	$0p_{1/2}$	$0p_{3/2}$	1	−0.62738	1^+	3^-	$0p_{3/2}$	$0d_{5/2}$	4	−0.01783
1^+	2^+	$0p_{1/2}$	$0p_{3/2}$	2	−0.44890	1^+	3^-	$0p_{3/2}$	$1s_{1/2}$	2	−0.01519
1^+	2^+	$0p_{3/2}$	$0p_{1/2}$	1	0.62744	1^+	3^-	$0d_{3/2}$	$0p_{1/2}$	2	−0.00874
1^+	2^+	$0p_{3/2}$	$0p_{1/2}$	2	−0.44895	1^+	3^-	$0d_{3/2}$	$0p_{3/2}$	2	−0.03579
1^+	2^+	$0p_{3/2}$	$0p_{3/2}$	1	−0.31358	1^+	3^-	$0d_{3/2}$	$0p_{3/2}$	3	−0.00461
1^+	2^+	$0p_{3/2}$	$0p_{3/2}$	3	−0.04167	1^+	3^-	$0d_{5/2}$	$0p_{1/2}$	3	−0.04673
1^+	2^+	$0d_{3/2}$	$0d_{3/2}$	1	0.00777	1^+	3^-	$0d_{5/2}$	$0p_{3/2}$	2	0.02004
1^+	2^+	$0d_{3/2}$	$0d_{3/2}$	3	0.00194	1^+	3^-	$0d_{5/2}$	$0p_{3/2}$	3	−0.00560
1^+	2^+	$0d_{3/2}$	$0d_{5/2}$	1	0.13445	1^+	3^-	$0d_{5/2}$	$0p_{3/2}$	4	−0.01783
1^+	2^+	$0d_{3/2}$	$0d_{5/2}$	2	0.04508	1^+	3^-	$1s_{1/2}$	$0p_{3/2}$	2	−0.01519

$$\phi_{\alpha+d}^{3b}(\mathbf{y}) = \langle \chi_d(\mathbf{x}) \,|\, \Psi(\mathbf{x}, \mathbf{y}) \rangle, \tag{9}$$

where $\chi_d(\mathbf{x})$ is the deuteron wave function, which can be numerically calculated using the RSC potential [25]. The wave function $\phi_{\alpha+d}^{3b}$ exhibits an asymptotic behaviour of the form $\exp(-kr)/r$, where $k = \sqrt{2\mu E_b/\hbar^2}$, $\mu = 4/3$, and the binding energy is $E_b = 1.474$ MeV. The spectroscopic amplitude associated with deuteron removal from ^{6}Li is

derived using the previously defined wave function as follows:

$$A^{3b} = \int \mathrm{d}y \, \phi(\mathbf{y})_{\alpha+d}^{3b}, \tag{10}$$

where the integration is performed over the relative coordinate y of the $\alpha + d$ system.

The angular distribution results from the CRC calculations are shown together with the experimental cross sections in Fig. 6 (a). It can be seen that the CRC calculations reproduce the experimental data well, except at angles beyond 50°. We suggest that other reaction mechanisms, such as knock-out or breakup processes, may contribute in this region and are not explicitly included in the CRC model. Nevertheless, the overall shape of the calculated cross section follows the experimental data, indicating a reasonable description of the reaction dynamics.

It is interesting to note that the contribution of the higher excited channels in the ^{6}Li + ^{12}C* system plays an important role in shaping the cross sections. This contribution becomes evident when the couplings from ^{6}Li + ^{12}C* to α + ^{14}N are included, compared to the direct DWBA transition from ^{6}Li + ^{12}C$_{gs}$ to α + ^{14}N (see Fig. 6). A particularly noticeable contribution originates from the ^{6}Li + ^{12}C(2^+) channel, which can be interpreted as a consequence of the slightly larger shell-model spectroscopic amplitude, $A^{SM} = 0.63$, compared to the value $A^{SM} = 0.58$ for the ground-state channel ^{6}Li + ^{12}C$_{gs}$ (see Table 2). In the case of the ^{12}C(^{6}Li, α)^{14}N reaction, the effects of strong CC interactions are clearly manifested and are shown to be significant contributors to the formation of the cross section. Similar effects have been reported for other nuclear reactions in various studies, such as Refs. [21, 39–40, 44].

Correlation of the three-body structure

It is well known that the ^{6}Li nucleus exhibits two different spatial configurations, which can be clearly seen in the plot of the probability density function

$$W(x,y) = |\Psi(x,y)|^2 x^2 y^2. \tag{11}$$

These two configurations – the "dumb-bell (DB)," characterized by a larger distance in the y coordinate than in x, and the "cigar-like (CIG)," where the x coordinate is much larger than y – are shown in Fig. 7(a). To isolate the DB configuration from the three-body wave function, we apply the operator (see, *e.g.*, in Ref. [20])

$$\hat{P}_{DB} = \frac{1}{1 + \exp(\xi/\xi_0)}, \tag{12}$$

while the corresponding operator for extracting the CIG configuration is given by

$$\hat{P}_{CIG} = 1 - \hat{P}_{DB} = \frac{1}{1 + \exp(-\xi/\xi_0)}, \tag{13}$$

where $\xi = (\gamma x - y)/\sqrt{1 + \gamma^2}$ and its parameters are taken as $\xi_0 = 0.2$ fm and $\gamma = 0.60$.

Using the relative-motion wave functions of the $\alpha + d$ system (Eq. 9) and applying the two different projection operators (Eq. 12 and 13) to the three-body wave function $\Psi(x,y)$, we estimated the individual contributions to the reaction cross section within the CRC. As mentioned above, only the S-wave component of the three-body configuration was used, as it contributes most significantly. The results of the CRC calculations with the two different spatial configurations are presented in Fig. 6(b). The DB configuration dominates the angular distribution across nearly the entire range, indicating that ^{6}Li predominantly behaves as an $\alpha + d$ cluster structure. The CIG configuration contributes less overall but still important to consider. At forward angles, where its contribution is strongest, its weight becomes comparable to that of the DB configuration, indicating that, in this region, the transfer predominantly occurs in the surface-localized part. At larger scattering angles, the CIG contribution
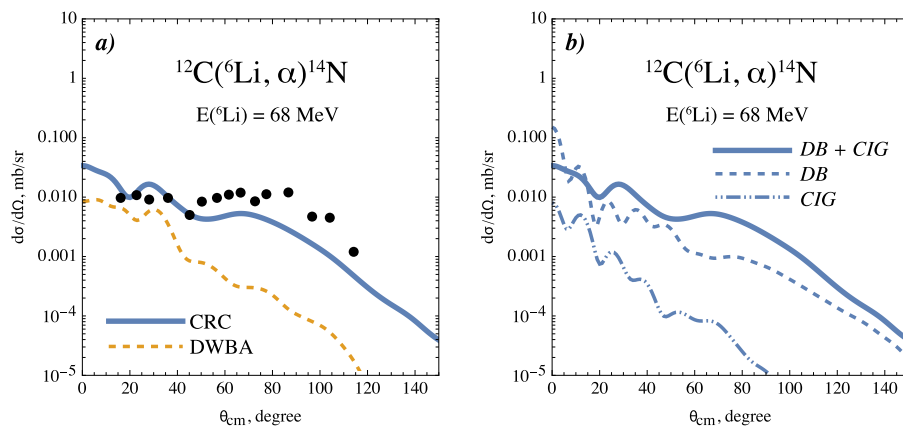

Fig. 6. (color online) Experimental cross-section data for the nuclear reaction ^{12}C(^{6}Li, α)^{14}N compared with those obtained with various reaction models. (a): Cross sections calculated within the CRC approach (solid line) and DWBA approach (dashed line). (b): The same CRC cross sections as in (a) but shown in terms of contributions from two different structural configurations of ^{6}Li: DB (dashed line) and CIG (dot-dashed line).

gradually diminishes. Nevertheless, despite their different behaviors and oscillations in the calculated cross sections, the interference of these two configurations provides a good overall description and reproduces the experimental data reasonably well, supporting the validity of the chosen structural model of ^{6}Li.

By splitting the relative-motion wave function $\phi_{\alpha+d}^{3b}$ into two components, it becomes possible to explain the dominance of the DB configuration. In addition to the greater height of the DB structure in the density distribution function (see Fig. 7 (a)), this dominance is reflected in the relative-motion wave function of the $\alpha + d$ system, as illustrated in Fig. 8 (a). It can be clearly seen that the DB structure accounts for approximately 80% of the integrated area $\int dy\, |\phi(y)|$, while the remaining 20% corresponds to the CIG structure.

The wave function $\phi_{\alpha+d}^{3b}$ used in the CRC calculations appears to have a slightly more compact shape compared with the phenomenological wave function $\phi_{\alpha+d}^{W}$ constructed using the Woods–Saxon potential. This tendency is

visible from the position of the node being slightly closer to zero and is also reflected in the rms radii, which are 2.49 fm for $\phi_{\alpha+d}^{3b}$ and 2.54 fm for $\phi_{\alpha+d}^{WS}$. The spectroscopic amplitude calculated with Eq. (10) is $A^{3b} = 1.07$, whereas the phenomenological wave function gives $A^{WS} = 0.97$. The three-body spectroscopic amplitude is therefore in closer agreement with the value of $A^{SM} = 1.06$ obtained within the framework of the translation-invariant shell model in Ref. [45] and $A^{SM} = 1.09$ calculated with KSHELL.

A comparison of the differential cross sections obtained with the two wave functions, $\phi_{\alpha+d}^{3b}$ and $\phi_{\alpha+d}^{WS}$, together with their corresponding spectroscopic amplitudes, is presented in Fig. 8 (b). Although the differences in the calculated cross sections are minor, the use of $\phi_{\alpha+d}^{3b}$ yields a slightly better agreement with the experimental data. This improvement is likely due to the fact that $\phi_{\alpha+d}^{3b}$ incorporates intrinsic three-body correlations of the ^{6}Li system, whereas the phenomenological $\phi_{\alpha+d}^{WS}$ does not fully include these correlations and represents the system in a
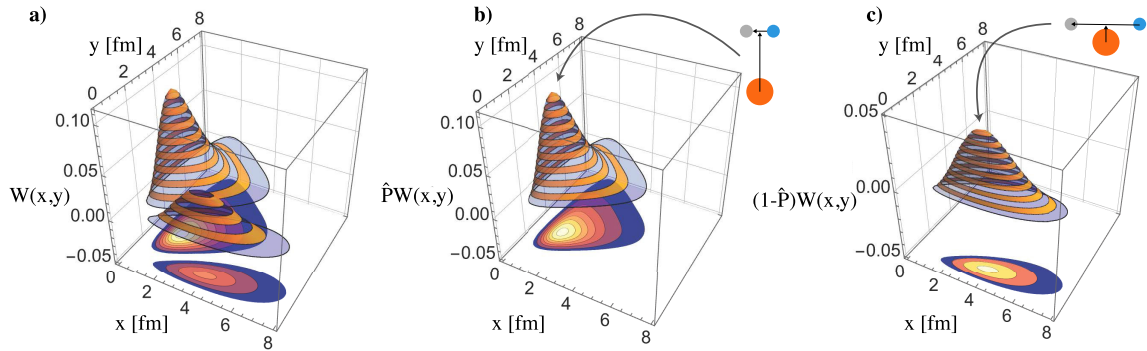

Fig. 7. (color online) 3D plots of the density distribution functions $W(x,y)$ of ^{6}Li within the three-body model, as implemented in the CRC calculations, shown in terms of two different spatial configurations: (a) total density distribution function; (b) DB configuration; (c) CIG configuration.
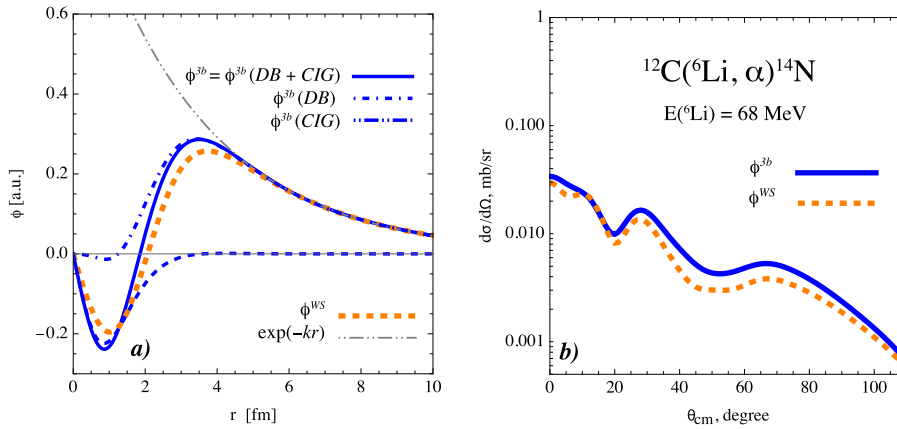

Fig. 8. (color online) Comparison of the relative-motion wave functions obtained from the three-body wave function $\phi_{\alpha+d}^{3b}$ with the phenomenological $\phi_{\alpha+d}^{WS}$: (a) the two spatial configurations (DB and CIG) both exhibit the same asymptotic behavior $\exp(-kr)/r$; (b) implementation of the two relative-motion wave functions, $\phi_{\alpha+d}^{3b}$ and $\phi_{\alpha+d}^{WS}$, in the CRC calculation. For clarity in the figure, the subscript $\alpha+d$ in $\phi_{\alpha+d}^{3b}$ and $\phi_{\alpha+d}^{WS}$ has been omitted.

more simplified manner. As a result, the three-body wave function provides a more physically motivated description of the reaction dynamics.

VI. CONCLUSION AND OUTLOOK

In this paper, both experimental and theoretical studies of the ^{12}C(^{6}Li, ^{6}Li)^{12}C and ^{12}C(^{6}Li, α)^{14}N reactions at a laboratory energy of 68 MeV are presented. The analysis was carried out within the OM, CC approach, and CRC framework, with particular attention to the cluster structure of the ^{6}Li nucleus.

The entrance channel was described using the double-folding potential based on the three-body nuclear matter density of ^{6}Li, while the exit channel was treated with the Woods–Saxon potential, whose parameters were adjusted to reproduce experimental elastic-scattering data. Spectroscopic amplitudes and relative-motion wave functions were obtained for both phenomenological and three-body models, and their influence on the calculated cross sections was systematically investigated.

The comparison of wave functions, including the DB and CIG spatial configurations, showed that the DB configuration dominates over most scattering angles, while the CIG configuration, though less significant overall, contributes notably at forward angles where the reaction is primarily surface-localized. This highlights the intrinsic three-body correlation characteristic of ^{6}Li, which are not fully captured by phenomenological models. The three-body wave function was found to be more compact and to provide spectroscopic amplitudes closer to values reported in earlier studies, leading to a more consistent description of the reaction dynamics.

Coupling effects from higher excited states and inelastic channels were shown to be crucial in shaping the cross sections, especially at backward angles. The inclu-

sion of these couplings in the CRC framework improved the agreement between calculations and experimental data, highlighting the necessity of considering both the internal structure of ^{6}Li and strong coupled-channels effects.

Overall, the results demonstrate that implementing the three-body model of ^{6}Li in CRC calculations provides a physically motivated and more accurate description of the reaction mechanisms. The interference between different spatial configurations and the explicit treatment of coupling effects are essential for understanding the underlying dynamics of light-ion nuclear reactions.

Building on the results obtained for ^{6}Li, a natural extension of this study is to investigate the ^{6}He + ^{12}C reaction. The ^{6}He nucleus, with its Borromean structure and two-neutron halo, presents a more pronounced three-body character and offers an excellent opportunity to probe the effects of extended matter distributions and neutron correlations on reaction mechanisms. Its loosely bound nature is expected to enhance coupling to continuum states and produce distinct signatures in transfer and breakup channels. Applying a similar three-body framework to ^{6}He would allow a direct comparison of spatial configurations − particularly the dineutron versus CIG modes − and their influence on observables. Moreover, such studies could provide tighter constraints on reaction models involving weakly bound neutron-rich systems, offering valuable insights into both nuclear structure and dynamics beyond the stability line.

References

[1]   O. Kiss , M. Grossi, P. Lougovski *et al.*, Phys.Rev. C **106**, 034325 (2022)
[2]   A. Amar and A. Ibraheem, Int. J. Mod. Phys. E **30**, 2150090 (2021)
[3]   G. Ropke, Phys.Rev. C **101**, 064310 (2020)
[4]   M. Egorov and V. Postnikov, Chin. Phys. C **45**, 014108 (2021)
[5]   B. Urazbekov, T. Issatayev, S. Lukyanov *et al.*, Chin. Phys. C **48**, 014001 (2024)
[6]   A. Solovyev, Phys. Atomic Nuclei **86**, 24 (2023)
[7]   S. Perrotta, M. Colonna and J. Lay, Phys. Rev. C **108**, 044614 (2023)
[8]   M. Zhukov, B. Danilin, D. Fedorov *et al.*, Phys. Rep. **231**, 151 (1993)
[9]   E. Braaten and H. W. Hammer, Phys. Rep. **428**, 259 (2006)
[10] A. Jensen, K. Riisager, D. V. Fedorov *et al.*, Rev. Mod. Phys. **76**, 215 (2004)
[11] C. D. Lin, Phys. Rep. **257**, 1 (1995)
[12] Y. Kanada-En'yo, H. Horiuchi and A. Ono, Phys. Rev. C **52**, 628 (1995)
[13] V. Kukulin, V. Krasnopol'sky, V. Voronche *et al.*, Nucl. Phys. A **417**, 128 (1984)
[14] J. Bang and C. Gignoux, Nucl. Phys. A **313**, 119 (1979)
[15] V. Starastsin, A. Demyanova, A. Danilov *et al.*, Eur. Phys. J. A **57**, 1 (2021)
[16] A. Azhibekov, S. Lukyanov, Y. E. Penionzhkevich *et al.*, Chin. Phys. C **48**, 114101 (2024)
[17] D. Nauruzbayev, V. Goldberg, A. Nurmukhanbetova *et al.*, Phys. Rev. C **96**, 014322 (2017)
[18] S. Lukyanov, M. Harakeh, M. Naumenko *et al.*, J. Phys.: Conf. Ser. **724**, 012031 (2015)
[19] U. Umbelino, K. Pires, R. Lichtenthäler *et al.*, Phys. Rev. C **99**, 064617 (2019)
[20] Y. T. Oganessian, V. Zagrebaev and J. Vaagen, Phys. Rev. C **60**, 044605 (1999)
[21] B. Urazbekov, A. Denikin, S. Lukyanov *et al.*, J. Phys. G:

Nucl. Part. Phys. **46**, 105110 (2019)

[22] B. Urazbekov, A. Denikin, S. Sakhiev *et al.*, Bulletin of the Russian Academy of Sciences: Physics **80**, 247 (2016)

[23] B. Urazbekov, A. Denikin, N. Itaco *et al.*, Phys. Atom. Nuclei **84**, 250 (2021)

[24] V. Kukulin, V. Pomerantsev, K. D. Razikov *et al.*, Nucl. Phys. A **586**, 151 (1995)

[25] B. Day , Phys. Rev. C **24**, 1203 (1981)

[26] V. Kukulin and V. Pomerantsev, Annals of Physics **111**, 330 (1978)

[27] B. Urazbekov 2021 *Manifestation of cluster structure of weakly bound light nuclei in direct nuclear reactions*, Ph.D. Thesis (Caserta: Universita degli Studi della Campania Luigi Vanvitelli, 2021)

[28] G. R. Satchler and W. G. Love, Phys. Rep. **55**, 183 (1979)

[29] V. Pomerantsev V and V. Kukulin V, 2015 Private communication: The groundstate parameters of the three boody wave function

[30] I. Tanihata, H. Hamagaki, O. Hashimoto O *et al.*, Phys. Rev. Lett. **55**, 2676 (1985)

[31] I. Sick, Phys. Lett. B **116**, 212 (1982)

[32] R. D. Woods and D. S. Saxon, Phys. Rev. **95**, 577 (1954)

[33] D. T. Khoa, Phys. Rev. C **63**, 034007 (2001)

[34] I. J. Thompson, Comput. Phys. Rep. **7**, 167 (1988)

[35] Y. Xu, Y. Han, J. Hu *et al.*, Phys. Rev. C **98**, 024619 (2018)

[36] J. Kelley, J. Purcell and C. Sheu, Nucl. Phys. A **968**, 71 (2017)

[37] M. Yasue, T. Tanabe, F. Soga *et al.*, Nucl. Phys. A **394**, 29 (1983)

[38] O. Aspelund, G. Hrehuss, A. Kiss *et al.*, Nucl. Phys. A **253**, 263 (1975)

[39] I. Thompson, M. Nagarajan, J. Lilley, Nucl. Phys. A **505**, 84 (1989)

[40] M. Harakeh, J. Van Popta, A. Saha *et al.*, Nucl. Phys. A **344**, 15 (1980)

[41] H. Abele, H. Hauser, A. Körber *et al.*, Zeitschrift für Physik A Atomic Nuclei **326**, 373 (1987)

[42] N. Shimizu, T. Mizusaki, Y. Utsuno *et al.*, Comput. Phys. Commun. **244**, 372 (2019)

[43] C. Yuan, T. Suzuki, T. Otsuka *et al.*, Phys. Rev. C **85**, 064324 (2012)

[44] S. Lukyanov, A. Azhibekov, T. Issatayev *et al.*, EPJ Web of Conferences **311**, 00017 (2024)

[45] A. Rudchik, E. Koshchy, A. Budzanowski *et al.*, Nucl. Phys. A **609**, 147 (1996)